Research Article

Enhanced photocatalytic activity of ZnO–NiO nanocomposites synthesized through a facile sonochemical route

U. S. Udayachandran Thampy[1] · A. Mahesh[1] · K. S. Sibi[1] · I. N. Jawahar[1] · V. Biju[1]

Abstract

Formation of heterostructures with p-type oxides such as NiO and CuO is one of the effective methods for improving the photocatalytic performance of ZnO. Such systems are often synthesized through template-based growth techniques that involve many steps. We have prepared ZnO–NiO composites through a facile, template-free, low-temperature sonochemical route. High-resolution transmission electron microscopy analysis indicates the formation of ZnO–NiO heterostructures. Photocatalytic activity of ZnO–NiO nanocomposites in the decomposition of methylene blue dye under solar irradiation is found to be much larger than that of both pure ZnO (1.26×10^{-2} min^{-1}) and NiO (0.31×10^{-2} min^{-1}) establishing synergistic effects. The rate constant increases with increase in the percentage of NiO in the composite and is 6.00×10^{-2} min^{-1} for sample with the highest percentage of NiO. Rate constants for the second and third runs are estimated to be 4.4×10^{-2} and 4.2×10^{-2} min^{-1} which are promising. The main mechanism of enhancement of photocatalytic activity of the composites is identified as the more effective separation of the photogenerated free charge carries due to the internal electric field at the ZnO–NiO interface. Sharp decrease in the relative intensity of the band–band emission of ZnO at ~380 nm in the case of composite samples and analysis of the relative position of the conduction band and valence band edges of ZnO and NiO support the proposed mechanism.

Keywords Photocatalyst · Zinc oxide · Nanocomposites · Heterostructures · Methylene blue

1 Introduction

Organic species present in the effluent from textile, pharmaceutical, paper and food industries are among the major pollutants that contaminate both surface and ground water. Photocatalytic degradation under solar irradiation is one of the efficient and cost-effective methods for treating water contaminated with organic pollutants. This technique is complementary to the conventional approaches of waste water treatment such as filtration and sedimentation [1]. Wide band-gap semiconductors such as TiO$_2$, ZnO, SnO$_2$, WO$_3$, Fe$_2$O$_3$, CdS and NiO are some of the most actively investigated systems as photocatalysts for water purification [2–11].

As a semiconducting metal oxide photocatalyst, nanostructured zinc oxide (ZnO) has attracted much attention as its performance is comparable to the commercially used TiO$_2$-based systems. However, ZnO-based photocatalysts have some drawbacks that include the relatively quick photogenerated charge carrier recombination and photocorrosion in aqueous media [12, 13]. A number of techniques have been employed for improving the performance of ZnO-based photocatalysts [12–26]. Doping with alkali/transition metals [14, 15] or non-metals (C, N,

✉ V. Biju, bijunano@gmail.com | [1]Department of Physics, University of Kerala, Karyavattom Campus, Thiruvananthapuram, Kerala 695581, India.

etc.) [16, 17] is one among them. ZnO-based heterostructures and composites with graphene [18], reduced graphene oxide [19], noble metals [20] and other metal oxides [21–28] are reported to show substantially improved photocatalytic activity. One of the highly effective methods for improving photocatalytic activity of ZnO is coupling with p-type oxides. Here, the formation of heterojunctions between the n-type ZnO and a suitable p-type semiconducting oxide can improve both photogenerated electron–hole pair separation efficiency and the light utilization capability.

Nanocomposites of semiconducting oxides such as ZnO, TiO_2 and CeO_2 are known to show very interesting chemical and physical properties and find applications in fields such as photocatalytic degradation of pollutants and harmful chemicals, electrochemical catalysts and non-enzymatic biosensors [29–34]. For instance, SnO_2–TiO_2 nanocomposite as an electrocatalyst for the oxidation of vitamin B6 is reported have lower over potential and larger signal response in comparison with pristine counterparts [29]. Also, mesoporous NiO–TiO_2 nanocomposite shows high sensitivity and selectivity as a redox active material in nonenzymatic glucose sensor [30]. In all these cases, synergistic effects due to surface related charge transfer mechanisms play a key role in improving the performance. Nanocomposites of ZnO, viz. ZnO–CeO_2, ZnO/γ-Mn_2O_3 and V_2O_5–ZnO, show much improved photocatalytic activity in the degradation reaction of organic pollutants such as methylene blue, methyl orange, phenol, and effluents from textile industry, where also charge transfer plays a key role [31–33]. It was also observed that the percentage of each constituent is very crucial in determining the performance of the final product [29–34].

Nickel oxide (NiO) is a p-type semiconducting oxide (band gap ~ 3.5 eV) with high hole mobility and low lattice mismatch with ZnO [23]. Hence, NiO is a suitable candidate for coupling with ZnO for the formation of p–n heterostructures. Many reports on the enhanced photocatalytic action of ZnO–NiO heterostructures synthesized by different methods have appeared in the literature in the recent past [21, 23, 25–27]. Such systems are often synthesized through template-based growth techniques that involve many steps. For instance, Luo et al. [23] reported a novel electrochemical route involving two steps for synthesizing ZnO–NiO heterostructures with improved photocatalytic activity. Here, the first step involved the electrodeposition of nanocrystalline Zn film on a Ni foam cathode. In the second step, Zn-coated Ni foam was annealed in air at high temperature (550 °C) to produce ZnO–NiO heterostructures [23]. Zhang et al. [21] had reported the synthesis of ZnO–NiO heterostructures through electrospinning process with improved photocatalytic activity. This method involves the use of

dedicated instrumentation, application of very high voltage (10 kV) and very careful optimization of experimental parameters to achieve the desired results. Xiao et al. [25] had reported a novel method for the synthesis of ZnO–NiO nanoheterojunctions through a chemical technique involving three steps. They had employed hydrothermally synthesized carbon spheres as supports for the growth of these heterostructures. These carbon spheres were thermally evaporated by calcination at high temperature (400 °C) in the final step [25]. There are also some reports on mixed oxides and nanocomposites of ZnO with p-type oxides such as NiO and CuO through simple template-free precipitation routes [27, 28, 35]. Noticeably, such reports do not mention the formation of p–n heterojunctions [27, 28, 35]. For instance, Sharma et al. [27] had prepared nanostructured ZnO–NiO mixed oxide powder with improved photocatalytic activity through a homogeneous precipitation method followed by high-temperature annealing in the range 300–700 °C. Facile chemical routes reported in the literature for the preparation of ZnO–NiO nanocomposites include one-pot solution processing followed by high-temperature annealing (300–700 °C) [28] and solvothermal process involving long process duration (12 h) [35].

It can be concluded from the literature survey that synthesis of ZnO–NiO heterostructures is most often done using techniques that involve multistep processes with numerous control parameters such as electrodeposition [23] or electrospinning [21]. Most of the techniques involve high processing temperatures [21, 23–25] with the lowest calcination temperature reported being 350 °C by Sharma et al. [27]. In the present work, nanostructured ZnO, NiO and ZnO–NiO composites with varying NiO concentrations are synthesized via a facile sonochemical method and the photocatalytic performance in the decomposition of methylene blue dye is studied under solar irradiation. Methylene blue ($C_{16}H_{18}ClN_3S$) is a model cationic dye most commonly employed for studying the efficiency of photocatalysts. Methylene blue was previously used as a medicine for diseases such as urinary tract infection, but the medicinal use was discontinued due to harmful effects on nervous system, cardiovascular system, etc. We observed that ZnO–NiO nanocomposites are much better photocatalysts than both the individual oxide counterparts in the decomposition of methylene blue and the activity increases with increase in the concentration of NiO. In the method reported herein, no template or support is used. The procedure is simple and does not involve many control parameters unlike in the case of electrodeposition or electrospinning processes. Further, low calcination temperature (250 °C) and short processing duration, viz. 3 h (mixing, sonication and calcination) compared to previously reported routes, are interesting from a practical view point [21, 23–25].

2 Experimental

Nanostructured ZnO, NiO and ZnO–NiO composites with varying concentrations of NiO were synthesized through a facile sonochemical route in aqueous medium. For synthesizing nanostructured ZnO, zinc acetate dihydrate (Zn $(CH_3COO)_2 \cdot 2H_2O$, Sigma-Aldrich Germany make, 97.7% purity) and sodium hydroxide (NaOH, Merck India make, 97% purity) were used as the starting materials. In a typical process, 300 ml of 0.1 M aqueous solutions of Zn $(CH_3COO)_2 \cdot 2H_2O$ (pH 6.6) and NaOH (pH 12.0) were thoroughly mixed. The pH of the solution after mixing was 7.5. The mixture was homogenized for 1 h using a magnetic stirrer. Ultrasonic waves were passed through this mixture for 1 h using an ultrasound probe sonicator (120 W, Vibronics India Pvt. Ltd. make). The white precipitate formed was thoroughly washed to remove any unreacted starting materials and was collected by centrifugation. It was dried at 60°C in a hot air oven. The dried sample was heat treated at 250 °C for 1 h to obtain pure zinc oxide (ZnO). This sample was coded as sample A.

For synthesizing nanostructured NiO, a similar procedure was followed by replacing Zn $(CH_3COO)_2 \cdot 2H_2O$ with nickel acetate $(Ni(OCOCH_3)_2 \cdot 4H_2O$, Sigma-Aldrich UK make, 99.9% purity). This sample was coded as sample B.

ZnO–NiO nanocomposites with varying percentages of NiO were synthesized by using $Zn(CH_3COO)_2 \cdot 2H_2O$ and $Ni(OCOCH_3)_2 \cdot 4H_2O$ solutions with different mole ratios, viz. 100:10, 100:15 and 100:20 as cation source and following the procedure already mentioned. Samples prepared with $Zn(CH_3COO)_2 \cdot 2H_2O$ and $Ni(OCOCH_3)_2 \cdot 4H_2O$ ratios, 100:10, 100:15 and 100:20, were coded as samples C, D and E, respectively.

X-ray diffraction (XRD) pattern of the samples was recorded using a Bruker D8 Advance X-ray diffractometer with Cu Kα (1.54056 Å) source in the range $2\theta = 10$–$80°$ with a step size of 0.02°. The morphology and microstructure of the samples were analysed using a ZEISS EVO-18 scanning electron microscope (SEM). Energy-dispersive spectra (EDS) of samples were recorded using an Oxford X-Max^N Silicon Drift Detector attached to the SEM instrument. Energy-dispersive X-ray dot mapping of Zn, Ni and O for one representative composite sample (sample D) was also carried out. A Tecnai G2 F30 S-TWIN 300 kV high-resolution transmission electron microscope (HRTEM) was used for the TEM analysis of sample E.

UV–visible diffuse reflectance spectra of the samples were recorded at room temperature using a Jasco V-750 Spectrophotometer. Room temperature photoluminescence (PL) emission spectra were recorded in a Horiba-FluoroMax 4 florescence spectrophotometer with 150-W

xenon lamp as the excitation source. The excitation was done at 320 nm.

Photocatalytic performance of the samples under solar irradiation was studied using methylene blue ($C_{16}H_{18}ClN_3S$, Merck India make) as a model organic pollutant. In a typical experiment, 0.05 g of the catalyst was suspended in 100 ml of methylene blue solution (0.03 mM). The solution was thoroughly mixed with the help of a magnetic stirrer in dark. Prior to irradiation, the dye–catalyst system was kept idle for 30 min in dark to achieve adsorption–desorption equilibrium. During irradiation, for analysing the progress of decomposition of the dye, 2.5 ml of the solution was withdrawn at regular intervals of 20 min and the absorption spectra were collected using a Shimadzu 2450 UV–visible absorption spectrophotometer. The absorption spectrum of the as prepared dye was used as control for estimating the degradation percentage. The progress of the dye degradation reaction was studied by analysing the intensity of 664 nm absorption peak of methylene blue. The degradation efficiency at time t was calculated using the relation, % Degradation $= \left[1 - \frac{C_t}{C_0}\right] \times 100$, where C_0 and C_t are the absorbance of the methylene blue solution before and after exposing to sun light.

3 Results and discussion

3.1 X-ray diffraction analysis

XRD patterns in Fig. 1 show the crystalline nature of the samples. For sample A, all the peaks could be perfectly indexed using standard values corresponding to the hexagonal wurtzite phase of ZnO (ICDD pattern no: 01-089-0510). Diffraction peaks corresponding to sample B are indexed to cubic NiO (ICDD pattern no: 00-047-1049). For the composite samples C, D and E, two sets of diffraction peaks are present which are attributed to hexagonal ZnO (ICDD pattern no: 01-089-0510) and cubic NiO (ICDD pattern no: 00-047-1049). For the composite samples with increase in the mole percentage of NiO, the diffraction peaks of NiO become more intense.

Rietveld refinement of the XRD patterns was carried out using DIFFRACT SUTE Plus-TOPAS software. The measured, calculated and difference patterns are included in Fig. 1. Background of each pattern was modelled by a Chebychev polynomial of order five. The refinement parameters were the scale factor, zero displacement, lattice parameters and strain. All parameters were refined simultaneously. The lattice parameters obtained together with R_{wp} values and goodness of fits are listed in Table 1.

Figure 1 shows good agreement between the measured and the refined XRD patterns. Average crystallite
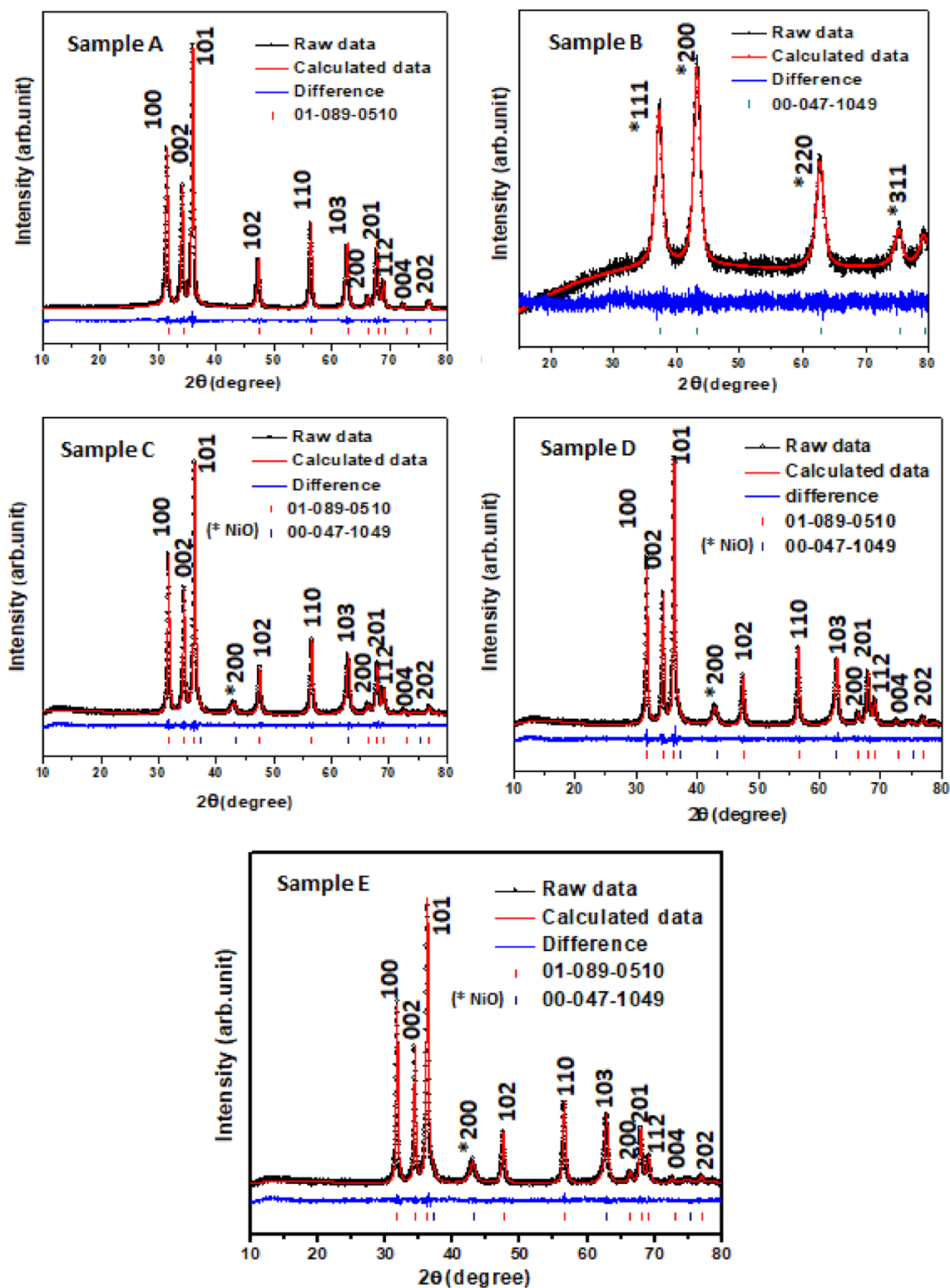
Fig. 1 XRD patterns of the samples with results of Rietveld refinement. * Sign shows peaks corresponding to NiO

size of samples (both ZnO and NiO in the case of composites) estimated from the full width at half maximum of the diffraction peaks obtained from the refinement procedure is also included in Table 1. For sample A (pure ZnO), the crystallite size is 20 ± 3 nm. Values of the crystallite size and error mentioned are the average of the

Table 1 Result of XRD analysis of the samples

Sample code	Reliability parameters		Structural parameters estimated				
			ZnO			NiO	
	R_{wp}	GOF	a (Å)	c (Å)	Crystallite size (nm)	a (Å)	Crystallite size (nm)
A	5.53	1.17	3.2487	5.2037	20 ± 3	–	–
B	12.44	1.04	–	–	–	4.1892	9 ± 1
C	9.60	1.28	3.2521	5.2086	19 ± 1	4.2117	9
D	8.87	1.21	3.2462	5.1089	21 ± 1	4.2104	12
E	8.97	1.19	3.2492	5.2061	23 ± 3	4.2020	18

crystallite sizes estimated from the five most intense peaks and the corresponding standard deviation, respectively. For sample B (pure NiO), the average crystallite size is 9 ± 1 nm. In the composite samples C and D, the average crystallite size of ZnO is almost same as that in pure sample (sample A), while for sample E the crystallite size is slightly larger, viz. 23 ± 3 nm. The crystallite size of cubic NiO in ZnO–NiO composites is calculated from the most intense peak. It can be seen that the average crystallite size of NiO in the composites increases from about 9 nm for sample C to 18 nm for sample E. The larger values of crystallite size for ZnO and NiO in sample E are probably due to the larger concentration of respective cation sources, viz. $Ni(OCOCH_3)_2 \cdot 4H_2O$ and $Zn(CH_3COO)_2 \cdot 2H_2O$ in the reaction mixture.

The lattice parameters obtained from the refinement procedure is also included in Table 1. Lattice parameters for pure ZnO sample (sample A) are $a = 3.2487$ Å and $c = 5.2037$ Å, which is very close to the standard values, viz. $a = 3.2488$ Å and 5.2054 Å. Lattice constants for ZnO in the composites first increase, then decrease and again increase with increase in the percentage of NiO. This irregular variation is due to the fact that the lattice parameters are affected by a number of factors such as the presence and concentration of defects, lattice strain and Coulomb interactions at the surface. For pure NiO sample, the lattice parameter is 4.1892 Å, which is slightly larger than the standard value, viz. 4.177 Å. In the composites also, the NiO crystallites show lattice expansion in comparison with bulk NiO and with increase in the average crystallite size, lattice expansion decreases. This is in agreement with previous reports on the lattice expansion in nanocrystalline NiO where the lattice expansion decreases with increase in the crystallite size [9, 36–38]. Lattice expansion in NiO has been attributed to the formation of point defects, grain-surface-relaxation effect, uncompensated Coulomb interactions, etc. [9, 36].

3.2 SEM, EDS and HRTEM analysis

SEM micrographs of the samples are shown in Fig. 2. All samples show agglomeration and surface morphology with noticeable roughness and voids which could be due to the expulsion of gases from the precipitate during calcination. The grains of the samples do not have any specific morphology such as rods, wires, spheres and sheets and resemble a fluffy mass with rough surface. EDS analysis reveals the presence of only Zn and O in sample A and only Ni and O in sample B. In the case of samples C, D and E, EDS analysis confirms the presence of Zn, Ni and O. EDS spectra of sample E are also included in Fig. 2. Elemental dot mapping of Zn, Ni and O in sample E is shown in Fig. 3. The elemental distribution of Zn, Ni and O shows that NiO is well mixed and uniformly distributed in the ZnO matrix.

TEM image of sample E shown in Fig. 4a is in confirmation with the nanocrystalline nature. The average particle size is ~ 20 nm (Fig. 4b). Figure 4c is a high-resolution image of a selected area. It can be seen that the interplanar distance of 0.25 nm is close to d-spacing of (101) planes of hexagonal ZnO, while interplanar distance of 0.21 nm is in agreement with the d-spacing of (200) planes of cubic NiO. The continuity of lattice fringes at clearly discernible interface of ZnO and NiO lattices is well evident from Fig. 4c. The distinguished interface and continuity of lattice fringes between NiO and ZnO nanoparticles indicate the formation of ZnO–NiO heterostructures [21, 25]. This leads to the inference that ZnO–NiO heterojunctions are formed in the composite samples synthesized though the present sonochemical route. Such heterojunctions are expected to increase the photogenerated electron–hole separation efficiency resulting in a fall in the intensity of photoluminescence emission and enhancement of photocatalytic activity [21–26].

Figure 4d shows the SAED pattern of the sample which is in agreement with the crystalline nature and the *hkl* planes corresponding to both ZnO and NiO are indexed.
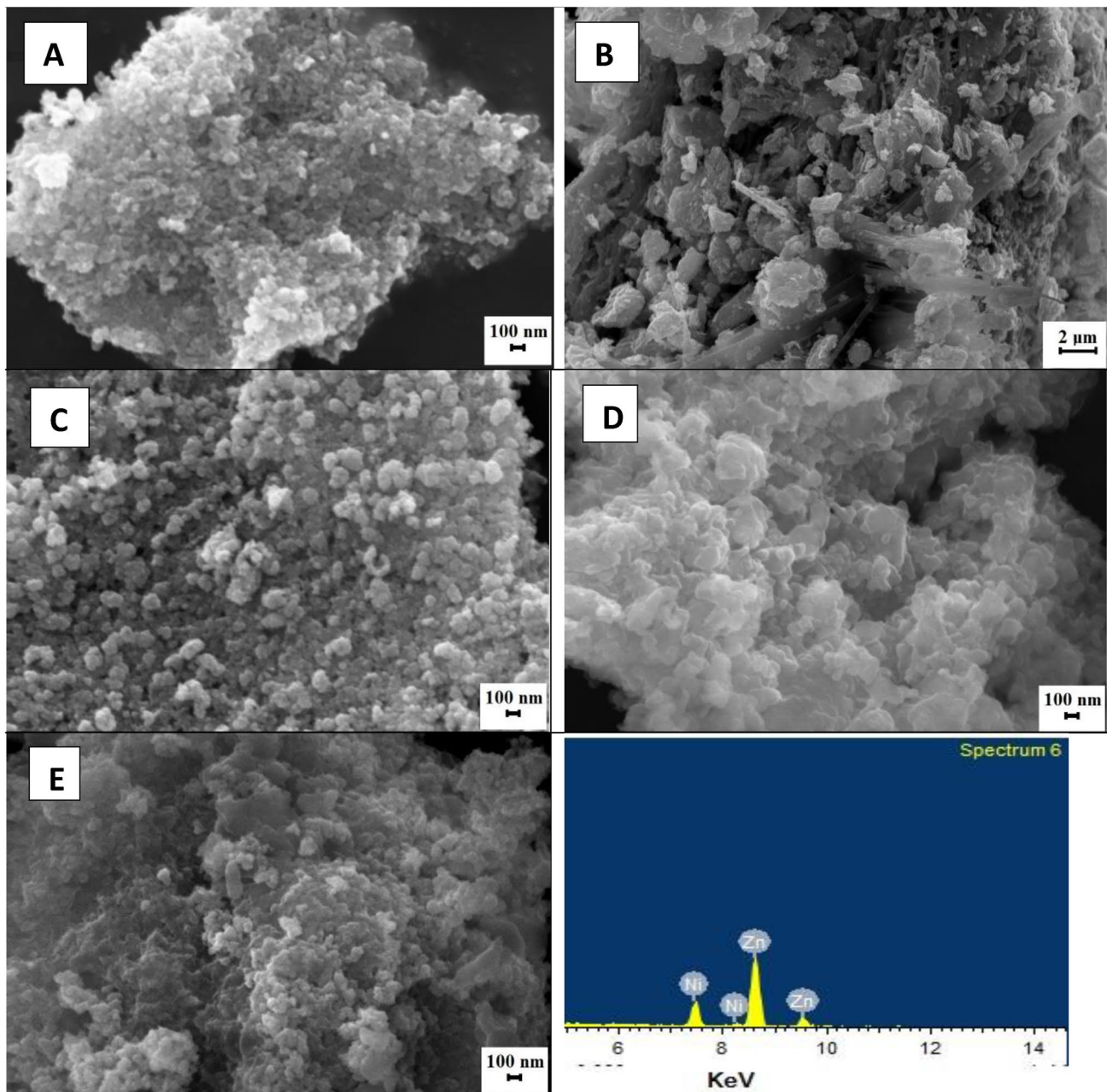
Fig. 2 SEM micrographs of samples **a**–**e** together with EDS spectra for one representative sample E

3.3 Analysis of UV–visible diffuse reflectance and photoluminescence emission spectra

Diffuse reflectance spectra of the samples are shown in Fig. 5a. For sample A, there is no reflection below 360 nm, above which the reflection suddenly increases. For sample B (NiO), the main reflectance peak starts above 314 nm, and in the higher wavelength (lower energy) region, some distinct peaks are present. In the spectra of composite samples, the most prominent reflection starts at about 368 nm which is very close to

the corresponding value for pure ZnO. Figure 5b is the Kubelka–Munk plots of the samples. By extrapolating the straight line region of the Kubelka–Munk plot, the band gap for sample A is obtained as 3.1 eV. This value is in agreement with those reported for nanostructured ZnO samples reported in the literature [39–42]. For sample B (pure NiO), the band gap is estimated to be 3.3 eV. Further, in the case of NiO, a number of peaks are clearly visible in the lower energy range, viz. 1.6–3 eV (Fig. 5c). These correspond to the d–d transitions of NiO [8]. These peaks are present in the spectra of composite samples
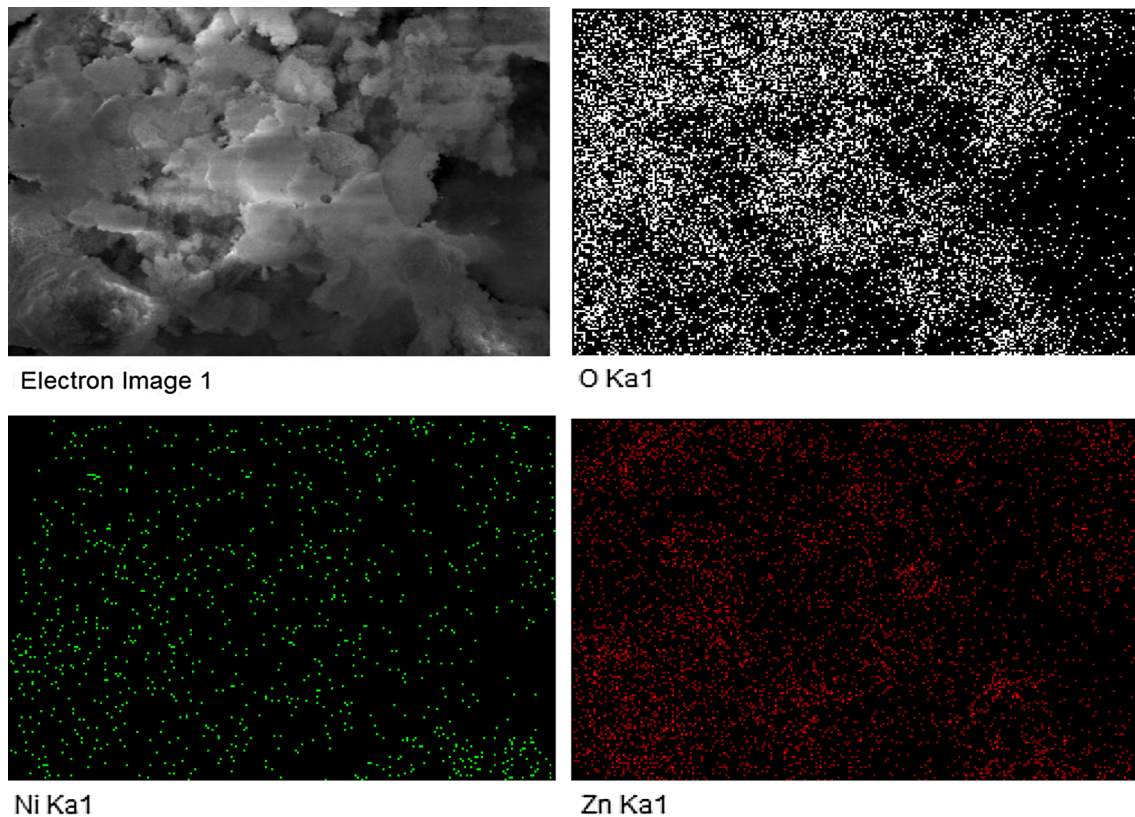
Fig. 3 Elemental dot mapping for sample D showing uniform distribution of ZnO and NiO

also (Fig. 5c). This means that due to the presence of NiO, the composite samples could absorb light energy even at lower frequencies, and hence, the light utilization ability for photocatalytic reaction will be better. The fundamental absorption edge for the composite samples C, D and E is 2.8, 3.0 and 3.1 eV, respectively.

Figure 5 d shows the photoluminescence spectra of the samples. The intensity of the photoluminescence emission is rather low for all samples. The spectra are normalized with respect to the band–band emission of sample A (pure ZnO). The fundamental band edge emission in ZnO is usually observed in the UV region at ~ 380 nm [40]. For the composite samples, with increase in the concentration of NiO, the ZnO band edge emission is very weak or almost completely absent. This indicates that with increase in the percentage of NiO, the probability of recombination of photoexcited free electrons and holes in ZnO decreases. Thus, the free charge carrier separation efficiency of composite samples is larger than that for pure ZnO sample which is advantageous for photocatalytic action [25, 43]. This observation is in good agreement with the formation of ZnO–NiO heterojunctions observed in the HRTEM analysis of sample E [21, 23].

3.4 Photocatalytic performance

Figure 6a–e shows, respectively, the UV–visible absorption spectra of methylene blue solution recorded at 20-min intervals during the decomposition under solar irradiation in the presence of photocatalysts A to E. From Fig. 6, the photocatalytic degradation is minimum for sample B (pure NiO sample), where the degradation is only 17.7% after 60 min. For pure ZnO catalyst (sample A), also the degradation is rather slow with ~ 53% degradation after 1 h. The decomposition of methylene blue dye in the presence of composite catalysts is relatively fast with sample E (with largest percentage of NiO) performing much better than all other samples. The percentage of degradation after 60 min for samples C and D is, respectively, ~ 63 and 89%. In the case of sample E, ~ 91% degradation is completed within 40 min, and with further elapse of time no more degradation occurs. Figure 7 shows the comparison of the photodegradation efficiency of the catalysts at different time intervals. One can clearly note both the enhanced performance of the composite samples in comparison with pure samples and the increase in the catalytic activity with increase in the percentage of NiO for the composites. Table 2 shows the performance of ZnO–NiO systems as photocatalysts reported in the literature [21, 24, 44–46].
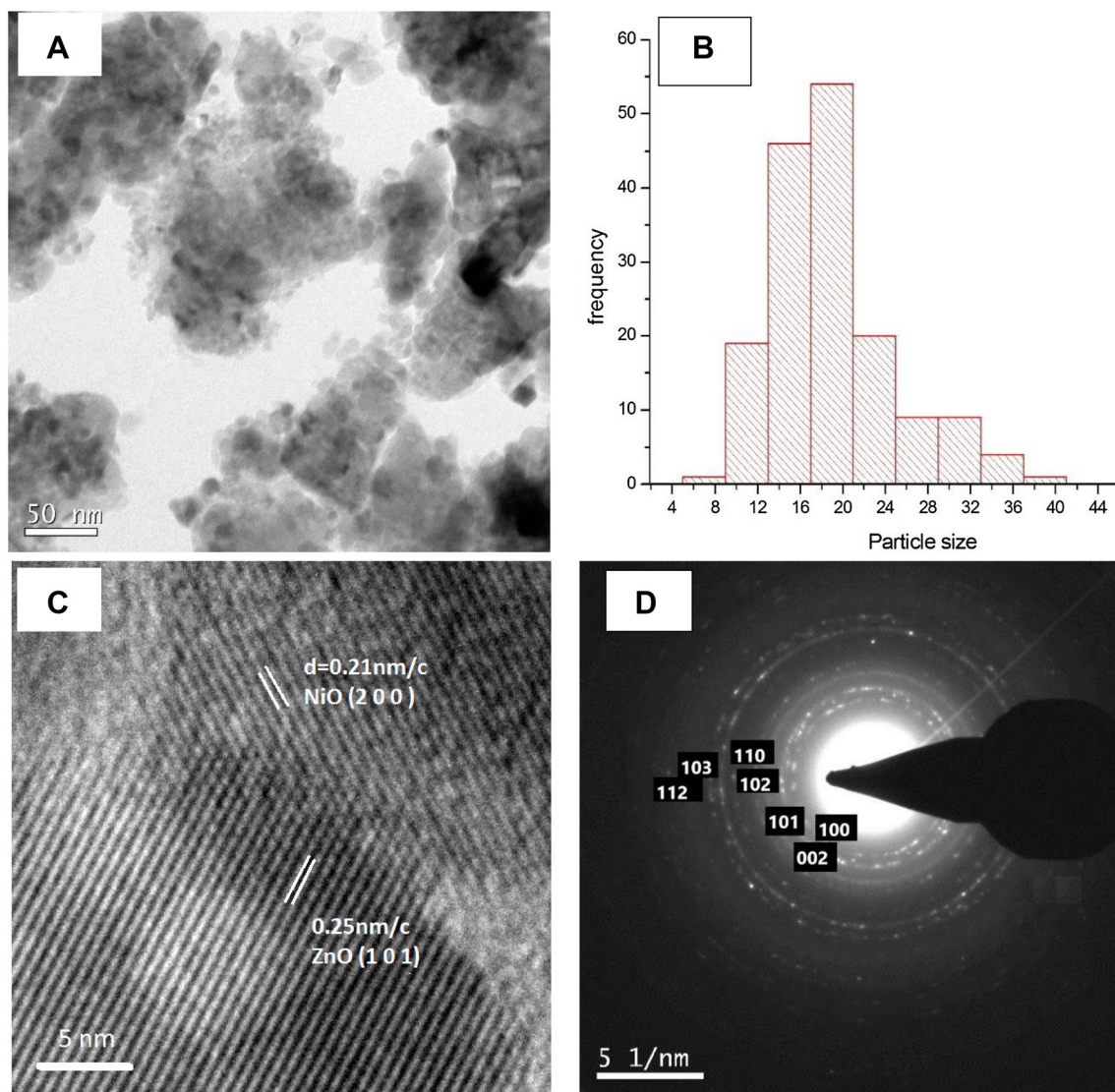
Fig. 4 Result of TEM analysis of sample E **a** TEM image, **b** particle size distribution, **c** HRTEM image confirming the formation of heterojunction, **d** SAED pattern

It can be seen that the performance of sample E is rather good in comparison with the reported values.

For comparing the performance of the catalysts quantitatively, the apparent first-order reaction rate constant k according to Langmuir–Hinshelwood model is calculated [47]. This model assumes that the heterogeneous catalytic action proceeds in three steps, viz. adsorption of the dye molecule on the surface of the photocatalyst, degradation and desorption of the final products. The rate constants are estimated to be 1.26×10^{-2}, 0.31×10^{-2}, 1.63×10^{-2}, 3.56×10^{-2} and 6.00×10^{-2} min^{-1} for samples A, B, C, D and E. The rate constant for the composite samples is larger than that of the pure samples. For the composites, the rate constant increases with increase in the percentage of NiO. More importantly, it can be seen that the rate

constant for pure NiO (sample B) is very small, one order of magnitude smaller than that for pure ZnO. Thus, the increase in the photocatalytic activity of composites is not due to the individual photocatalytic activity of ZnO or NiO crystallites present and is certainly due to some kind of synergistic effect. HRTEM analysis (Sect. 3.2) had clearly shown the formation of ZnO–NiO heterojunctions in the composites, while the decrease in the intensity of PL emission peak corresponding to the band-to-band transition of ZnO (Sect. 3.3) was in support of this inference. This could possibly enhance the photocatalytic activity of the composites.

The reusability test for sample E which has the best performance is shown in Fig. 8a. It can be seen that in the second and third cycles, the degradation efficiency values are
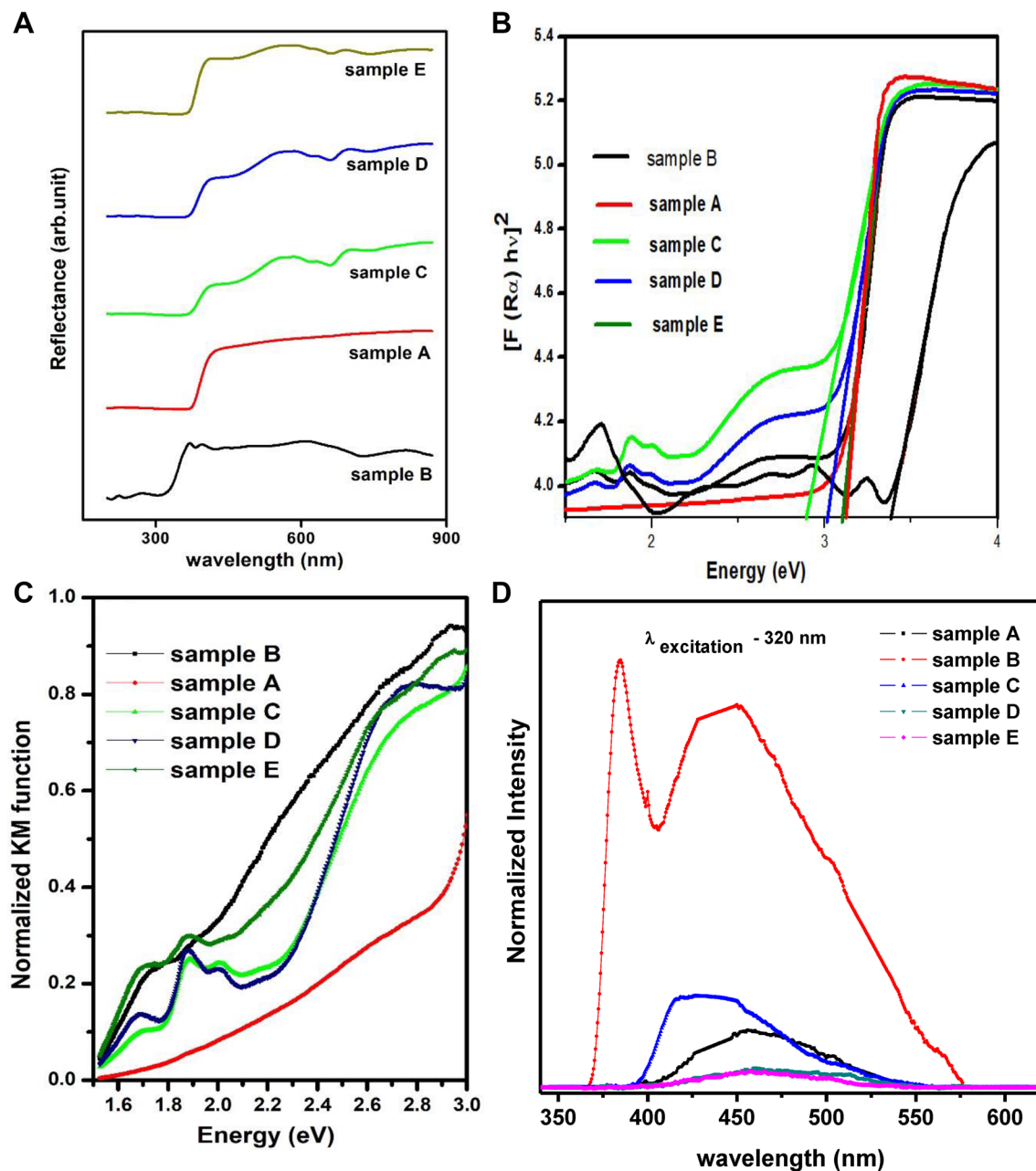
Fig. 5 **a** Diffuse reflectance spectra, **b** determination of band gap of samples, **c** absorption in the composite samples in the lower energy region, **d** photoluminescence spectra of samples normalized with respect to the band–band emission of sample A

83% and 81% which are marginally low in comparison with the first run, viz. 91%. The pseudo-first-order rate constants for second and third runs are estimated as 4.4×10^{-2} and 4.2×10^{-2} min^{-1}, respectively. Even during the third run, the rate constant is almost four times higher than the rate constant of pure ZnO which is promising from an application point of view.

We have also tested the performance of sample E in the degradation of methyl orange ($C_{14}H_{14}N_3NaO_3S$; 0.01 mM solution), and the results for three runs are shown in Fig. 8b. Methyl orange is an anionic dye and is known to be much more stable compared to methyl blue. It was observed that the efficiency of the photocatalyst is relatively low with only 34% of degradation occurring in 80 min in the first run. During the second and third runs, only 25% and 22% of degradation occurred. The rate constants during the first, second and third runs are 5×10^{-3}, 3×10^{-3} and 2×10^{-3} min^{-1}, respectively.
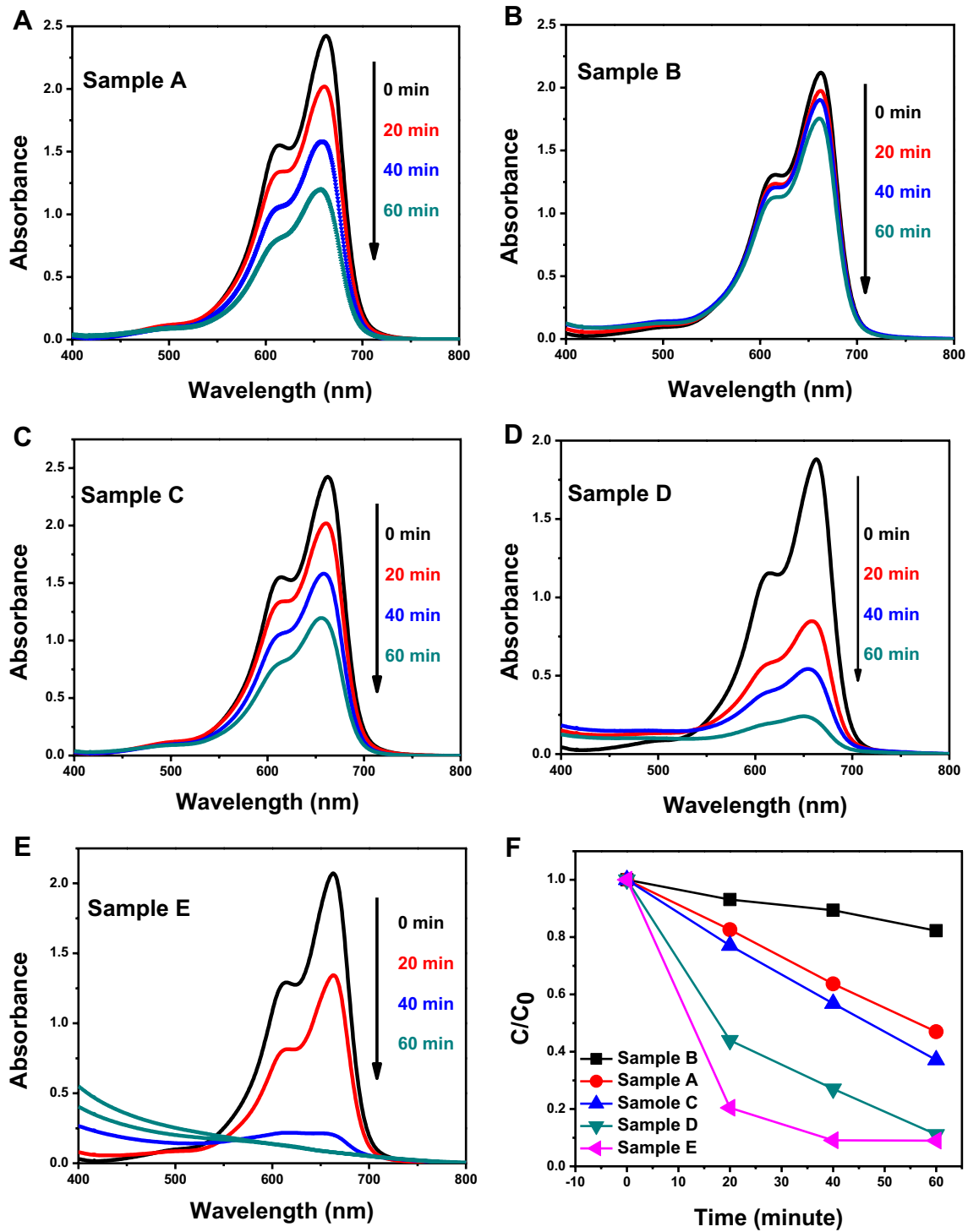
Fig. 6 **a**–**e** Absorption spectra of methylene blue dye during photocatalyzed degradation reaction under solar irradiation for samples A–E. **f** Plot of C/C_0 with time

In order to study the mechanism of enhanced photocatalytic activity in the composite samples, an analysis of the relative position of the conduction band and valence band edges of ZnO and NiO is required [31–33]. The conduction band (E_{CB}) and valence band (E_{VB}) edges for ZnO and NiO with respect to normal hydrogen electrode potential (NHE) are estimated using the equations

$$E_{CB} = \chi - E^e - 0.5E_g \qquad (1)$$
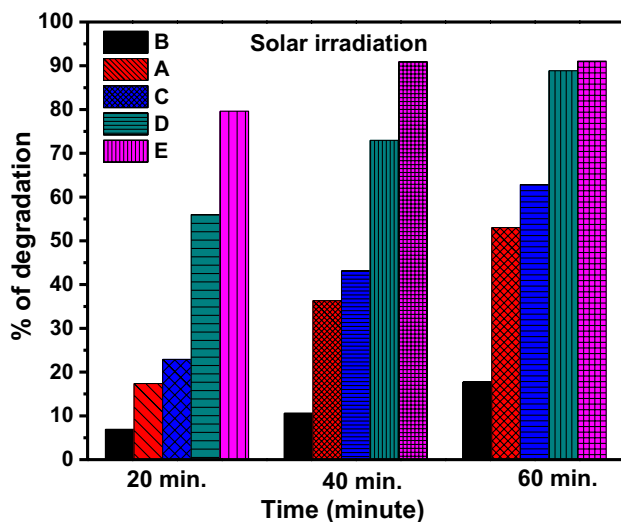
Fig. 7 Percentage degradation of methylene blue dye at different time intervals in the case of catalysts A–E

$$E_{VB} = \chi - E^e + 0.5E_g \qquad (2)$$

Here, χ is the electro-negativity of the semiconductor, E^e is the energy of free electrons with respect to NHE, and E_g is the band gap measured from DRS spectra. Electronegativity χ of a semiconductor with composition $A_nB_mC_l$ can be estimated using the formula

$$\chi = \left[\chi(A)^n + \chi(B)^m + \chi(C)^l \right]^{1/(n+m+l)} \qquad (3)$$

Here, $\chi(A)$, $\chi(B)$ and $\chi(C)$ are, respectively, the electro-negativities of elements A, B and C.

Using these relations, the conduction band edge and valence band edge for pure ZnO are estimated to be −0.10 eV/NHE and 3.0 eV/NHE, respectively. Corresponding values for pure NiO are −0.39 eV/NHE and 2.91 eV/NHE. The band edge positions for ZnO and NiO are shown in Fig. 8a. As the CB edge of ZnO is located at a lower energy in comparison with the CB edge of NiO, photoexcited electrons in conduction band could be transferred to CB of ZnO, thereby increasing the concentration of free electrons. These free electrons could lead to the formation of O_2^- leading to decomposition of the dye. Similarly, the position of the valence band edges permits the transfer of holes from ZnO to NiO. However, the sharp decrease in the intensity of emission peak corresponding to band–band electronic transition of ZnO and the result of HRTEM study indicate the formation of p–n heterojunctions. This contributes to more effective separation of free charge carriers which increases the life time of free charge carriers and enhances the photocatalytic activity depicted as follows.

Fermi level for ZnO (n-type) is just below the conduction band, while that for NiO (p-type) is just above the valence band (Fig. 9a). Thus, when ZnO and NiO are coupled, at the heterojunction, a depletion region is formed with positively and negatively charged regions in the ZnO and NiO sides, respectively, such that Fermi levels of both semiconductors are aligned [48, 49]. This results in an internal electric field from the n-side to the p-side as shown in Fig. 9b. The mechanism of enhancement of photocatalytic activity due to the formation of heterostructures is schematically depicted in Fig. 9b and can be explained as follows. Due to the presence of this internal electric field, when the valence electrons in ZnO are excited due to absorption of photons, the corresponding holes in the valence band are transferred to the valence band of NiO. Similarly, free electrons due to the photoexcitation in NiO are driven to the conduction band of ZnO [21, 49]. Thus, the internal electric field at the junction hinders the recombination of photogenerated free electrons and holes in the catalyst. This in turn enhances the concentration of both free electrons and holes on the surface of the catalyst leading to an enhancement in the catalytic activity. This model is well supported by the drastic fall in the intensity of the band–band emission of ZnO centred at 380 nm

Table 2 Performance of ZnO–NiO systems as photocatalysts reported in the literature

Description of sample	Organic pollutant	Quantity of photocatalyst and light source	Degradation rate	References
Electrospun NiO/ZnO nanofibers	Rhodamine blue (10 mg/l)	0.01 g in 100 ml; 50 W high-pressure Hg vapour lamp	86.6% after 50 min	[21]
NiO/ZnO nanocomposites	Methylene blue and methyl orange (0.005 mol)	2.8 g/l; 450 W medium-pressure Hg vapour lamp	74 to 80% after 10 min	[44]
NiO/ZnO nanocomposites	Metronidazole (drug capsule) (1 mg/l)	2.5 g/l; 35 W moderate-pressure Hg vapour lamp	87% after 150 min	[45]
Cubic structure NiO-hexangular structure ZnO	Methyl orange (10 mg/l)	100 mg in 200 ml; 500 W high-pressure Hg lamp	Complete decoloration of reaction mixture within 25 min	[24]
Cubic NiO particles on flower-like ZnO	Methyl orange (10 mg/l)	100 mg in 200 ml; 500 W high-pressure Hg lamp	99% degradation after a 20-min irradiation	[46]

Fig. 8 C/C_0 as a function of time for three runs for sample E **a** methylene blue and **b** methyl orange
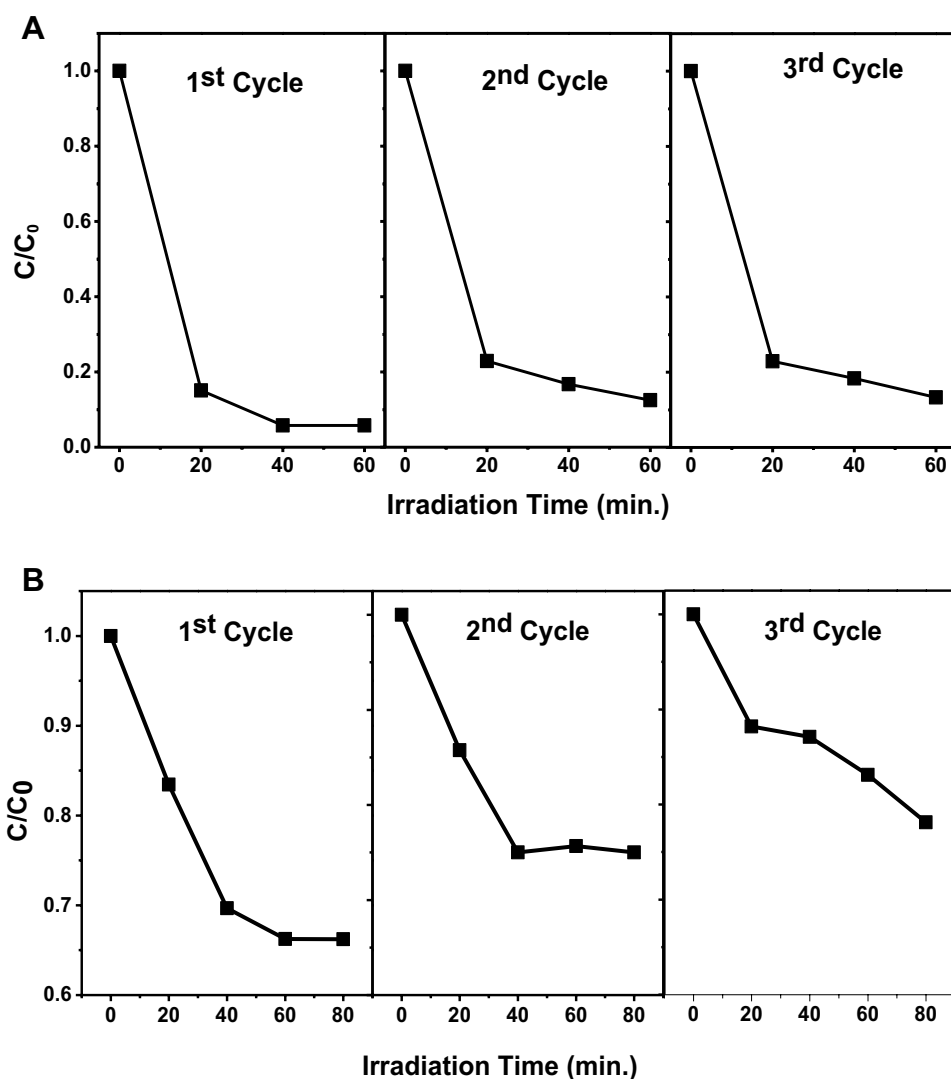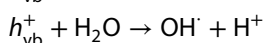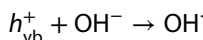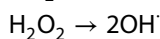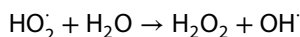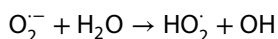

in the composite samples (Fig. 5d) [41]. Thus, in the present case though the electronic band gap is not much varied in the composites in comparison with pure ZnO, the charge separation efficiency is increased due to the formation of p–n heterojunctions. Over and above the decrease in the free charge carrier recombination efficiency, the d–d transitions in NiO due to the absorption of photons with energies lower than the band gap also contribute to the photocatalytic action of the composite due to the formation of holes in the valence band of NiO [9].

The decomposition of the methylene blue dye is due to the formation of both super oxide anion radical $O_2^{\cdot-}$ and hydroxide radicals $OH^{\cdot}$ at the surface of the catalysts. The formation of $O_2^{\cdot-}$ radicals due to the action of free electrons associated with the valence band of ZnO can be explained by the scheme given as follows [3].

$$e_{cb}^- + O_2 \rightarrow O_2^{\cdot-}$$
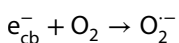
Here, e_{cb}^- represents a photogenerated free electron in the conduction band which according to the model proposed preferably resides in ZnO. The formation of $OH^{\cdot}$ could be either due to the action of this oxide anion radical or due to the action of holes in the valence band [1, 3, 4, 25, 26]. Both schemes are depicted as follows.

$$O_2^{\cdot-} + H_2O \rightarrow HO_2^{\cdot} + OH$$
$$HO_2^{\cdot} + H_2O \rightarrow H_2O_2 + OH^{\cdot}$$
$$H_2O_2 \rightarrow 2OH^{\cdot}$$
$$h_{vb}^+ + OH^- \rightarrow OH^{\cdot}$$
$$h_{vb}^+ + H_2O \rightarrow OH^{\cdot} + H^+$$

Here, h_{vb}^+ represents a hole in the valence band which preferably resides in NiO according to the model. Both $O_2^{\cdot-}$ and $OH^{\cdot}$ radicals are strong oxidizing agents that
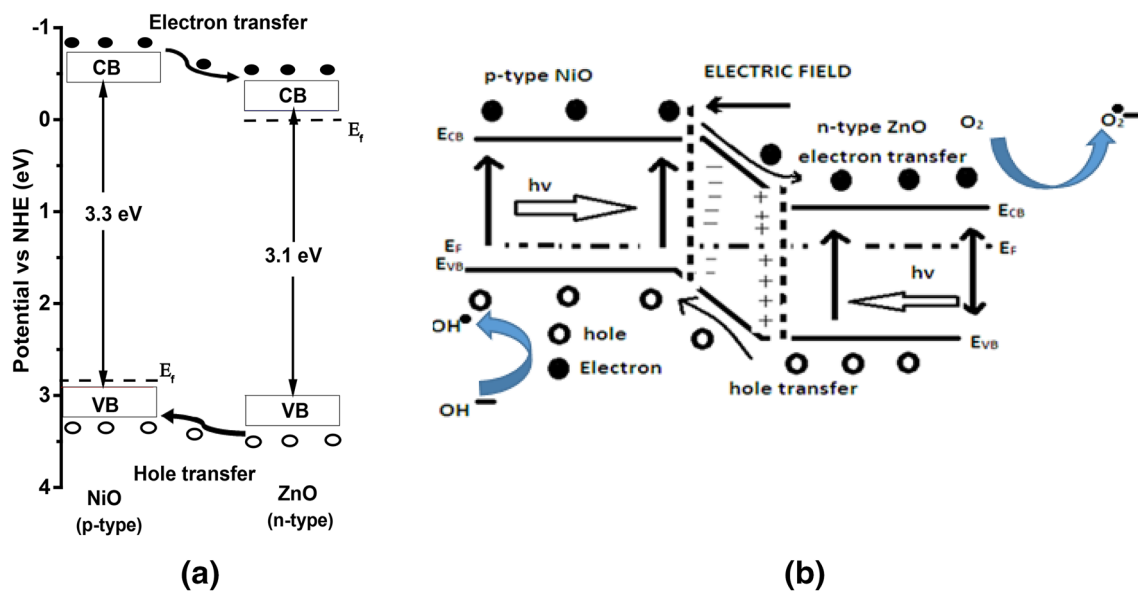
Fig. 9 **a** Position of valence band and conduction band edges of ZnO and NiO with respect to normal hydrogen electrode and **b** the charge separation mechanism at ZnO–NiO interface leading to formation of free radicals

could effectively cause the degradation of the methylene blue dye into less harmful species such as CO_2 and H_2O.

4 Conclusions

Nanostructured ZnO, NiO and ZnO–NiO composites with varying percentages of NiO are successfully synthesized through a novel facile sonochemical route. Advantages of this synthesis route in comparison with previously reported ones include template-free nature, low calcination temperature (250 °C) and relatively small processing duration (3 h). HRTEM studies indicate the formation of ZnO–NiO heterojunctions in the composites. Though the band gap of the composites is not much varied from those of pure ZnO, absorption below the bad gap in the visible range due to the d–d transitions in NiO is favourable for photocatalytic activity. The band-to-band emission of ZnO is suppressed in the composites as a consequence of the formation of p–n heterojunctions. Pseudo-first-order rate constant for the photocatalytic degradation reaction for sample E having largest fraction of NiO is 6.00×10^{-2} min^{-1}, almost six times larger than that for ZnO. Further, the sample has good performance when reused with rate constant of 4.4×10^{-2} and 4.2×10^{-2} min^{-1}, respectively, for second and third runs. The improved photocatalytic action for composite samples is attributed to an increase in the photogenerated charge carrier separation efficiency due to the formation of ZnO–NiO heterojunctions. Analysis of the relative position of the conduction band and valence band edges of ZnO and NiO also supports the proposed photogenerated charge carried separation mechanism. It was also observed that in the decomposition reaction of methyl orange, the catalytic efficiency for sample E is $k = 5 \times 10^{-3}$ min^{-1}.

Compliance with ethical standards

Conflict of interest On behalf of all the authors, the corresponding author states that there is no conflict of interest.

References

1. Hoffmann MR, Martin ST, Choi W, Bahnemann DW (1995) Environmental applications of semiconductor photocatalysis. Chem Rev 95:69–96

2. Wang X, Wang X, Zhao J, Song J, Su C, Wang Z (2018) Surface modified TiO$_2$ floating photocatalyst with PDDA for efficient adsorption and photocatalytic inactivation of Microcystis aeruginosa. Water Res 131:320–333

3. Girish Kumar S, Koteswara Rao KSR (2015) Zinc oxide based photocatalysis: tailoring surface-bulk structure and related interfacial charge carrier dynamics for better environmental applications. RSC Adv 5:3306–3351

4. Sudheer Kumar KH, Dhananjaya N, Reddy Yadav LS (2018) *E. tirucalli* plant latex mediated green combustion synthesis of ZnO nanoparticles: structure, photoluminescence and photocatalytic activities. J Sci Adv Mater Devices 3:303–309

5. Jia X, Liu Y, Wu X, Zhang Z (2014) A low temperature situ precipitation route to designing Zn-doped SnO$_2$ photocatalyst with enhanced photocatalytic performance. Appl Surf Sci 311:609–613

6. Paik T, Cargnello M, Gordon TR, Zhang S, Yun H, Lee JD, Woo HY, Oh SJ, Kagan CR, Fornasiero P, Murray CB (2018) Photocatalytic hydrogen evolution from substoichiometric colloidal WO$_{3-x}$ nanowires. ACS Energy Lett 3:1904–1910

7. Marques RG, Ferrari-Lima AM, Slusarski-Santana V, Fernandes-Machado NRC (2017) Ag$_2$O and Fe$_2$O$_3$ modified oxides on the photocatalytic for treatment of pulp and paper wastewater. J Environ Manag 195:242–248

8. Xiong J, Du X, Cheng G, Yang H, Chen J, Douc S, Li Z (2018) One dimensional hierarchical nanostructures composed of CdS nanosheets/nanoparticles and Ag nanowires with promoted photocatalytic performance. Inorg Chem Front 5:903–915

9. Maniammal K, Madhu G, Biju V (2018) Nanostructured mesoporous NiO as an efficient photocatalyst for degradation of methylene blue: structure, properties and performance. Nano Struct Nano Objects 16:266–275

10. Sathishkumar S, Parthibavarman M, Sharmila V, Karthik M (2017) A facile and one step synthesis of large surface area SnO$_2$ nanorods and its photocatalytic activity. J Mater Sci: Mater Electron 28:8192–8196

11. Parthibavarman M, Sathishkumar S, Jayashree M, Boopathi Raja R (2019) Microwave assisted synthesis of pure and Ag doped SnO$_2$ quantum dots as novel platform for high photocatalytic activity performance. J Cluster Sci 30:351–363

12. Zhang Z, Chen G, Bahnemann DW (2009) Photoelectrocatalytic materials for environmental applications. J Mater Chem 19:5089–5121

13. Zhang H, Zong R, Zhu Y (2009) Photocorrosion inhibition and photoactivity enhancement for zinc oxide via hybridization with monolayer polyaniline. J Phys Chem C 113:4605–4611

14. Benhebal H, Chaib M, Leonard AL, Lambert SD, Crine M (2012) Photodegradation of phenol and benzoic acid by sol–gel-synthesized alkali metal-doped ZnO. Mater Sci Semicond Process 15:264–269

15. Saleh R, Djaja NF (2014) Transition-metal-doped ZnO nanoparticles: synthesis, characterization and photocatalytic activity under UV light. Spectrochim Acta Part A Mol Biomol Spectrosc 130:581–590

16. Ansari SA, Ansari SG, Foaud H, Cho MH (2017) Facile and sustainable synthesis of carbon-doped ZnO nanostructures towards the superior visible light photocatalytic performance. New J Chem 41:9314–9320

17. Rangel R, Cedeno V, Ramos-Corona A, Gutiésrrez R, Alvarado-Gil JJ, Ares O, Bartolo-Pérez P, Quintana P (2017) Tailoring surface and photocatalytic properties of ZnO and nitrogen-doped ZnO nanostructures using microwave assisted facile hydrothermal synthesis. Appl Phys A 123:552

18. Xue B, Zou Y (2018) Uniform distribution of ZnO nanoparticles on the surface of graphene and its enhanced photocatalytic performance. Appl Surf Sci 440:1123–1129

19. Qin J, Zhang X, Yang C, Cao M, Ma M, Liu R (2017) ZnO microspheres-reduced graphene oxide nanocomposite for photocatalytic degradation of methylene blue dye. Appl Surf Sci 392:196–203

20. Raji R, Sibi KS, Gopchandran KG (2018) ZnO: Ag nanorods as efficient photocatalysts: sunlight driven photocatalytic degradation of sulforhodamine B. Appl Surf Sci 427:863–875

21. Zhang Z, Shao C, Li X, Wang C, Zhang M, Liu Y (2010) Electrospun nanofibers of p-type NiO/n-type ZnO heterojunctions with enhanced photocatalytic activity. ACS Appl Mater Interfaces 2:2915–2923

22. Shukla P, Shukla JK (2018) Facile sol-gel synthesis and enhanced photocatalytic activity of the V$_2$O$_5$–ZnO nanoflakes. J Sci Adv Mater Devices 3:452–455

23. Luo C, Li D, Wu W, Zhanga Y, Pan C (2014) Preparation of porous micro–nano-structure NiO/ZnO heterojunction and its photocatalytic property. RSC Adv 4:3090–3095

24. Liu Y, Li G, Mi R, Denga C, Gao P (2014) An environment-benign method for the synthesis of p-NiO/n-ZnO heterostructure with excellent performance for gas sensing and photocatalysis. Sens Actuators, B 191:537–544

25. Xiao M, Lu Y, Li Y, Song H, Zhu L, Ye Z (2014) A new type of p-type NiO/n-type ZnO nanoheterojunctions with enhanced photocatalytic activity. RSC Adv 4:34649–34653

26. Li B, Wang Y (2010) Facile synthesis and photocatalytic activity of ZnO–CuO nanocomposites. Superlattices Microstruct 47:615–623

27. Sharma RK, Kumar D, Ghose R (2017) Synthesis of nanocrystalline ZnO–NiO mixed metal oxide powder by homogeneous precipitation method. Ceram Int 42:4090–4098

28. Kim KH, Yoshihara Y, Abe Y, Kawamura M, Kiba T (2017) Morphological characterization of sphere-like structured ZnO–NiO nanocomposites with annealing temperatures. Mater Lett 186:364–367

29. Manoj D, Rajendran S, Qin J, Sundaravadivel E, Yola ML, Atar N, Gracia F, BoukherroubR G-PMA, Kumar Gupta V (2019) Heterostructures of mesoporous TiO$_2$ and SnO$_2$ nanocatalyst for improved electrochemical oxidation ability of vitamin B6 in pharmaceutical tablets. J Colloid Interface Sci 542:45–53

30. Rajendran S, Manoj D, Raju K, Dionysiou DD, Naushad M, Gracia F, Comejo L, Gracia-Pinila MA, Ahamad T (2018) Influence of mesoporous defect induced mixed valent NiO (Ni^{2+}Ni^{3+})-TiO$_2$ nanocomposite for non-enzymatic glucose biosensors. Sens Actuators B Chem 264:27–37

31. Rajendra S, Khan MM, Gracia F, Qin J, Gupta VK, Arumainathan S (2016) Ce^{3+}-ion-induced visible-light photocatalytic degradation and electrochemical activity of ZnO/CeO$_2$ nanocomposite. Sci Rep 6:31641

32. Saravanan R, Gupta VK, Narayanan V, Stephen A (2014) Visible light degradation of textile effluent using novel catalyst ZnO/γ-Mn$_2$O$_3$. J Thaiwan Inst Chem E 45:1910–1917

33. Saravanan R, Gupta VK, Mosquera E, Gracia F (2014) Preparation and characterization of V$_2$O$_5$/ZnO nanocomposites system for photocatalytic application. J Mol Liq 198:409–412

34. Mishara J, PattanayakD S, Das AA, Mishara DK, Sahoo NK (2019) Enhanced photocatalytic degradation of cyanide employing Fe-porphyrin sensitizer with hydroxyapatite palladium doped TiO$_2$ nano-composite system. J Mol Liq 287:110821

35. Aslani A, Arefi MR, Babapoor A, Amiri A, Beyki-Shuraki K (2011) Solvothermal synthesis, characterization and optical properties of ZnO, ZnO–MgO and ZnO–NiO, mixed oxide nanoparticles. Appl Surf Sci 257:4885–4889

36. Ghosh M, Biswas K, Sundaresan A, Rao CNR (2006) MnO and NiO nanoparticles: synthesis and magnetic properties. J Mater Chem 16:106–111

37. Duan WJ, Lu SH, Wu ZL, Wang YS (2012) Size Effects on properties of NiO nanoparticles grown in akali salts. J Phys Chem C 116:26043–26051

38. Kremenović A, Jancar B, Ristic M, Vasic MV, Rogan J, Pacevski A, Antic B (2012) Exchange-bias and grain-surface relaxations in nanostructured NiO/Ni induced by a particle size reduction. J Phys Chem C 116:4356–4364

39. Hvam JM (1973) Exciton–exciton interaction and laser emission in high-purity ZnO. Solid State Commun 12:95–97

40. Özgür Ü, AlivovYa I, Liu C, Teke A, Reshchikov MA, Doğan S, Avrutin V, Cho SJ, Morkoç H (2005) A comprehensive review of ZnO materials and devices. J Appl Phys 98:041301

41. Wang C, Wu D, Wang P, Ao Y, Hou J, Qian J (2015) Effect of oxygen vacancy on enhanced photocatalytic activity of reduced ZnO nanorod arrays. Appl Surf Sci 325:112–116

42. Djurišić AB, Leung YH, Tam KH, Fhsu Y, Ding L, Ge WK, Zhong YC, Wong KS, Chan WK, Tam HL, Cheah KW, Kwok WM, Phillips DL (2007) Defect emissions in ZnO nanostructures. Nanotechnology 18:095702

43. Zhang X, Qin J, Xue Y, Yu P, Zhang B, Wang L, Liu R (2014) Effect of aspect ratio and surface defects on the photocatalytic activity of ZnO nanorods. Sci Rep 4:4596

44. Hameed A, Montini T, Gombac V, Fornasiero P (2009) Photocatalytic decolourization of dyes on NiO–ZnO nano-composites. Photochem Photobiol Sci 8:677–682

45. Derikvandi H, Nezamzadeh-Ejhieh A (2017) Increased photocatalytic activity of NiO and ZnO in photodegradation of a model drug aqueous solution: effect of coupling, supporting, particle size and calcination temperature. J Hazard Mater 321:629–638

46. Tian F, Liu Y (2013) Synthesis of p-type NiO/n-type ZnO heterostructure and its enhanced photocatalytic activity. Scripta Mater 69:417–419

47. Klubnuan S, Suwanboon S, Amornpitoksuk P (2016) Effects of optical band gap energy, band tail energy and particle shape on photocatalytic activities of different ZnO nanostructures prepared by a hydrothermal method. Opt Mater 53:134–141

48. Habibi-Yangjeh A, Shekofteh-Gohar M (2017) Novel magnetic Fe_3O_4/ZnO/$NiWO_4$ nanocomposites: enhanced visible-light photocatalytic performance through p-n heterojunctions. Sep Purif Technol 184:334–346

49. Saravanan R, Karthikeyan S, Gupta VK, Sekaran G, Narayanan V, Stephen A (2013) Enhanced photocatalytic activity of ZnO/CuO nanocomposite for the degradation of textile dye on visible light illumination. Mater Sci Eng, C 33:91–98